Optimal location of a synthetic jet on an airfoil for stall control

Régis Duvigneau, Alexander Hay, Michel Visonneau

Optimal Location of a Synthetic Jet on an Airfoil for Stall Control

R. Duvigneau[1]
Regis.Duvigneau@sophia.inria.fr

A. Hay
hay@vt.edu

M. Visonneau
Michel.Visonneau@ec-nantes.fr

Laboratoire de Mécanique des Fluides
CNRS UMR6598,
Equipe Modélisation Numérique,
Ecole Centrale de Nantes,
rue de la Noë, 44321 Nantes, France

This study deals with the optimization of the location of a synthetic jet on the suction side of an airfoil to control stall. The optimal location is found by coupling a time-accurate flow solver with adaptive mesh refinement/coarsening techniques and an automatic opti-mization algorithm. The flow and jet are modeled by the unsteady Reynolds-averaged Navier-Stokes equations (URANSE) with a near-wall low-Reynolds number turbulence closure. An unstructured grid refinement/coarsening method is used to automatically generate meshes adapted to the presence of the synthetic jet at a prescribed location. An optimization algorithm modifies the location of the synthetic jet to determine the best actuator location to increase the time-averaged lift for high angles of attack. The pro-posed methodology is applied to optimize the location of a synthetic jet on the suction side of the NACA 0012 airfoil at a Reynolds number Re=2□10^6 and incidences of 18 deg and 20 deg. Finally, a physical analysis of the influence of the synthetic jet location on the control efficiency is proposed to provide some guidelines for practical jet positioning.

1 Introduction

Flow control using synthetic jets has been an active topic of research for many years. Indeed, it was shown experimentally that flows can be modified by introducing jets with ad hoc properties to obtain desired characteristics [1]. Some numerical investigations of lift enhancement using synthetic jets found in the literature use time-accurate solutions of the Reynolds-averaged Navier-Stokes equations. Wu et al. [2] investigated post-stall lift enhancement for a NACA 0012 airfoil using a normal suction/blowing jet located at 2.5% of the chord and found that lift enhancement in the post-stall regime can be achieved, as was reported in experiments. Steady blowing as well as oscillatory jet actuations were simulated by Donovan et al. [3] and compared to experimental measurements. The same configuration was also studied by Ekaterinaris [4], who tested some different jet parameters.

These studies provide useful information to help engineers who need to control the flow around an airfoil to delay stall. However, some questions remain open: For a particular airfoil, at a given Reynolds number and specific angles of attack, where should a synthetic jet be located to delay stall? Which frequency should be employed? What is the minimum jet velocity requires to achieve satisfactory flow control?

To answer these questions, we tested coupling between a time-accurate flow solver and an optimization algorithm and applied it to delay stall on a NACA 0015 airfoil [5,6]. The simultaneous optimization of the jet frequency, amplitude, and orientation significantly increased the control efficiency (+34% C_L). However, the influence of the jet location on stall delay was not taken into account in this previous study because it was not possible, at that time, to automatically generate grids adapted to variable jet locations.

To overcome this limitation and provide a methodology allowing the automatic optimization of the jet location, we proposed coupling of a time-accurate flow solver, an adaptive mesh refinement/coarsening technique, and an automatic optimization algorithm. The numerical methods used in the flow solver are described in the first section. Then, we provide details on the grid refinement/coarsening techniques used to automatically generate a mesh adapted to the jet location. The optimization procedure is finally presented. Although our ultimate goal is simultaneous optimization over all parameters (frequency, amplitude, direction, and location), we prefer at the present time to focus on the optimization of the jet location only. In the following section, the procedure is applied to determine the optimal location of a synthetic jet to delay stall for the NACA 0012 airfoil at Reynolds number Re$=2\times10^6$ for two values of the angle of attack. Finally, the characteristics of the controlled flow are studied to understand the relationship between jet location and control efficiency.

2 Flow Solver

The numerical simulation of stall control is performed by the ISIS-CFD flow solver, developed by EMN (Equipe Modélisation Numérique, i.e., CFD Department of the Fluid Mechanics Laboratory). The prediction of massively separated flows, such as those encountered in stall control, is a difficult task because results are highly dependent on the choice of turbulence and transition models for which knowledge and numerical modeling are very incomplete. Although large eddy simulation (LES) approaches may be more suitable for such flows, we have chosen to use the unsteady Reynolds-averaged Navier-Stokes equations (URANSE). Indeed, for practical and cost-effectiveness considerations, LES is still prohibitive for high Reynolds numbers, particularly in a design optimization framework.

The incompressible unsteady Reynolds-averaged Navier-Stokes equations can be written as (using the generalized form of Gauss' theorem)

$$\frac{\partial}{\partial t}\int_V \rho dV + \int_S \rho(\vec{U}-\vec{U}_d)\cdot\vec{n}dS = 0 \qquad (1a)$$

$$\frac{\partial}{\partial t}\int_V \rho U_i dV + \int_S \rho U_i(\vec{U}-\vec{U}_d)\cdot\vec{n}dS = \int_S (\tau_{ij}I_j - pI_i)\cdot\vec{n}dS + \int_V \rho g_i dV \qquad (1b)$$

where V is the domain of interest, or control volume, bounded by a closed surface S moving at a velocity $\vec{U}_d$ with a unit outward normal vector $\vec{n}$. $\vec{U}$ and p represent, respectively, the velocity and

[1]Corresponding author. INRIA — Projet Opale, 2004 route des lucioles, BP 93, 06902 Sophia-Antipolis, France.

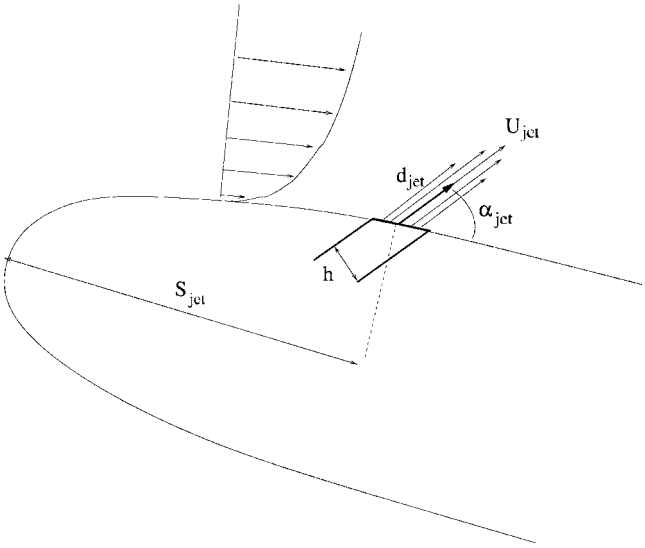

Fig. 1 Configuration of the computations

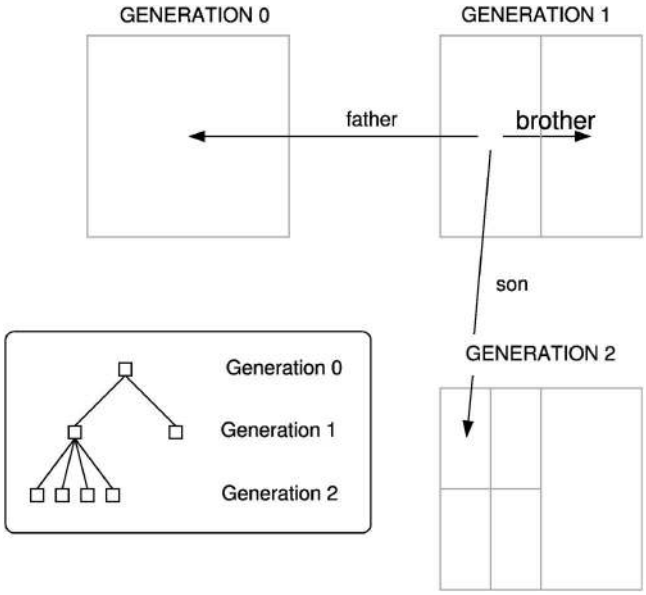

Fig. 2 Relationship between the different generations of elements

pressure fields. τ_{ij} and g_i are the components of the viscous stress tensor and the gravity, whereas I_j is the identity vector whose components vanished, except for the component j, which is equal to unity.

All flow variables are stored at the geometric center of arbitrary shaped cells. Volume and surface integrals are evaluated with second-order accurate approximations. Numerical fluxes are reconstructed on mesh faces by linear extrapolation of integrand from the neighboring cell centers. A centered scheme is used for the diffusion terms, whereas a combination of upwind and centered schemes is applied to the convective terms. The combination used results from a blending based on a continuous exponential scheme involving the signed Peclet number at the face [7].

A pressure equation is obtained in the spirit of Rhie and Chow [8]. Momentum and pressure equations are solved in a segregated manner like in the SIMPLE coupling procedure [9].

A second-order backward difference scheme is used to discretize time. All spatial terms appearing in Eqs. (1*a*) and (1*b*) are treated in a fully implicit manner.

Several turbulence closures are available in the flow solver, ranging from linear eddy-viscosity models to full second-order closures. We have opted for the near-wall low-Reynolds number $k-\omega$ SST model of Menter [10] because it behaves satisfactorily for separated flows over airfoils. Turbulent variables k and ω are obtained by solving transport equations discretized in a manner similar to that used for the momentum equations.

The synthetic jet actuator is modeled as a suction/blowing-type boundary condition. We prescribe the following velocity distribution at the jet lips:

$$\vec{U} = U_{\text{jet}} \sin(2\pi N_{\text{jet}} t) f(\xi) \vec{d}_{\text{jet}} \tag{2}$$

where $\vec{d}_{\text{jet}}$ is a unit vector in the direction of the jet. α_{jet} is the angle between $\vec{d}_{\text{jet}}$ and the wall (Fig. 1). $f(\xi)$ is the velocity distribution across the jet inlet. $f(\xi)=\sin^2(\xi)$ is used to accurately describe the jet flow [3]. For the turbulent variables, normal gradients of value zero are imposed at the jet boundary for both k and ω. The jet width is usually very small with respect to the length scale of the problem. Thus, the grid should be especially fine in the vicinity of the slot to provide a detailed description of the jet boundary layer interaction. Such grids are generated automatically using the local adaptive mesh procedure described in Sec. 3.

3 Adaptive Techniques

3.1 Principle. An automatic local adaptive mesh procedure (*h*-refinement) is well suited to track the temporal evolution of the jet and to maintain a fine computational grid around it. Moreover, an automatic grid adaptation frees the user from the tedious task of generating a mesh suitable for any jet position. Indeed, using mesh adaptation, one can start from a coarse uniform grid that is refined thanks to an explicit error indicator. We use a simple refinement indicator based on the distance to the jet location. Thus, the cell size within a sphere surrounding the jet slot can be controlled to provide a precise description of the jet velocity distribution and sufficient resolution of its interaction with the wall boundary layer. This section presents the basic features of the adaptive procedure.

3.2 Data Structure. An appropriate data structure is required to ensure a simple yet flexible and fast mesh adaptation. Our local mesh adaptation procedure is based on the notion of a relationship between the successive generations of elements of the grids and stores the information in a treelike data structure (see Fig. 2). This approach is used to efficiently store and retrieve data for control volumes, of arbitrary shapes as well as for all mesh faces. They are presented here only for the control volumes but similar notions apply to the faces of the grids [11,12]. The initial mesh consists of elements of generation 0, and a first refinement step leads to the birth of elements of generation 1. A control volume tagged for refinement becomes a father and is split into several sons (which share a brotherly relationship while the father and its sons form a family). Further refinement steps will induce genesis of elements of generation 2 and so on. It should be emphasized that this structure does not restrict the generality of the grid adaptation process because it does not require information about how the elements are refined. Besides, negative generations can exist because cell agglomeration can coarsen the initial grid when required [11]. Such a data structure permits one to address several problems at once. First, the unrefinement of a family (thus, of a previously refined cell) becomes straightforward since it corresponds to the recovery of its father (and also the destruction of its sons). Thus, the refinement/unrefinement process becomes fully dynamic and quick to achieve. Second, it guarantees exact recovery of the initial mesh if refinement is no longer necessary in some area of the computational grid, as is the case with unsteady problems.

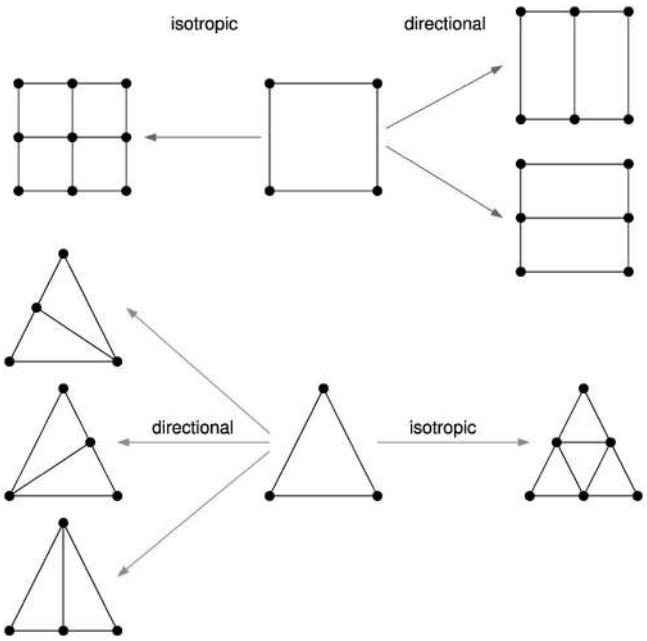

Fig. 3 Refinement of two-dimensional volumes

3.3 Grid Alteration. During the refinement process, each control volume tagged for refinement is split into several smaller ones of the same topology. Thus, a son inherits the topology of its father and the difference is restricted to cell size. This ensures that the initial desired local mesh quality is preserved everywhere throughout the simulation. For two-dimensional grids, as illustrated in Fig. 3, the refinement process can occur with a possible directional sensitivity for flows with simple features.

In the present study, meshes are only refined in the tangential direction to the wall. Indeed, by construction, grids are already very fine in the normal direction to the wall. We emphasize that adapted grids require no specific treatment in the flow solver. A nonrefined neighbor of a refined cell presents a so-called hanging node, which is accounted for naturally by our face-based finite-volume method: a face with a hanging node is simply seen as several smaller faces.

Special treatments are necessary when refining a curved boundary surface because two requirements have to be fulfilled when a new node is added on the surface of the body:

- The node must be placed on the exact geometry, which should be described either analytically or by a CAD description readable by the flow solver.
- For convex boundaries and high aspect ratio cells, the inclusion of a new node on the surface of the body should not generate neighboring cells with negative volumes.

To avoid ill-conditioned near-wall cells, we move the grid in accordance with the discrete boundaries' deformation by generalizing the mesh deformation tools already included in the flow solver and previously used for shape optimization studies [13,14]. For two- and three-dimensional cases, a lineal and torsional spring analogy is employed to control the deformation of the grid. The association of lineal and torsional springs provides a powerful mesh deformation tool that maintains the grid quality near the wall even for high deformations [15].

4 Optimization Procedure

4.1 Optimization Loop. Design optimization consists of maximizing an objective function f that depends on the design variables D and the flow variables $Q(D)$. The governing equations of the flow $R[D,Q(D)]=0$ are considered as constraints that must be satisfied at each step of the design procedure. Some bound constraints must be added to the problem to find a realistic solution. Thus, the variation domain of design variables is usually closed. From a mathematical point of view, the problem may be expressed as

$$\text{Maximize } f[D,Q(D)]$$

$$\text{Constrained to } R[D,Q(D)]=0$$

$$L_i \le D \le L_s$$

In the present work, the objective function is the time-averaged lift coefficient C_l of the airfoil. It is evaluated after all transient effects have vanished, by integrating the instantaneous lift coefficient over several flow cycles

$$f[D,Q(D)]=\frac{1}{t_2-t_1}\int_{t_1}^{t_2} C_l[D,Q(D)]dt \tag{3}$$

In practice, the integration is performed over five flow cycles. Numerical experiments have shown that this interval of integration is large enough to ensure that time-dependency effects be negligible. The design variable D is the location of the synthetic jet s_{jet} on the suction side of the airfoil (see Fig. 1). Other parameters, such as frequency, amplitude, and direction, are fixed during optimization to focus on the analysis of the location dependency. Therefore, the optimization procedure consists of several unsteady flow simulations for a synthetic jet with different locations, whose value is modified by the optimization algorithm. Thus, the design procedure is described by the following steps:

1. Generation of a baseline grid X_0
2. Initialization of the design variables D_0
3. Step $k=0$
4. Generation of an adapted grid $X_k(D_k)$
5. Unsteady simulation of the flow $Q_k(D_k)$
6. Evaluation of the lift $f(D_k,Q_k(D_k))$
7. Correction ΔD_k by the optimization algorithm
8. Update $D_{k+1}=D_k+\Delta D_k$, $k=k+1$
9. Go to step 4

until the convergence of the design variables is achieved.

4.2 Optimization Strategy. Gradient-based optimizers are popular because of their efficiency since they can reach a maximum of the objective function in a number of evaluations lower than zero-order methods. However, some difficulties arise when used on complicated realistic problems. The evaluation of the derivatives of the objective function for a sophisticated simulation process is a nontrivial task. Their evaluation is usually based on an adjoint formulation that relies on the differentiation of the flow solver [16]. This task is tedious when high-order discretization schemes on unstructured grids are used or complex turbulence models are employed. This approach often requires a priori simplification of the problem, neglecting turbulence sensitivities for instance, or using first-order discretization schemes, which provides an approximated gradient [16]. All in all, this approach appears restricted to moderately complicated problems and its use for massively separated flows remains a challenge.

To overcome these limitations, we chose a derivative-free algorithm that is easier to implement in a complex numerical framework. Furthermore, this approach is less sensitive to numerical noise because no information about the derivatives is needed to predict the optimization path. The number of flow evaluations required is higher than that needed by gradient-based methods, but it remains reasonable, as soon as the number of design variables is low, which is the case in the present study.

4.3 Algorithm. We chose an optimizer relying on an iteratively updated quadratic interpolating model of the objective function, inspired from the work of Marazzi and Nocedal [17]. Assuming that the value of the objective function is known as a set of sample points, including the best point x_k, a local quadratic interpolating model q_k is built at each optimization step k. For a quadratic model, $(1/2)(n+1)(n+2)$ sample points are needed, where n is the number of design variables

$$q_k(x_k+s) = f(x_k) + g_k^T s + \tfrac{1}{2} s^T H_k s \tag{4}$$

The unknown coefficients g_k and H_k are determined by solving a linear system, expressing the interpolation condition at the sample points.

Assuming that the model q_k is valid in a ball of radius ρ_k centered at x_k, called the trust region, a subproblem is solved at each iteration to minimize q_k in this region

$$\text{Minimize} \quad q_k(x) \quad x \in \mathcal{R}^n$$

$$\text{Constraint to} \quad \|x - x_k\| \leq \rho_k \tag{5}$$

Contrary to response surface techniques that rely on a global and approximated model using a large number of sample points, the present method minimizes a local and interpolated model at each iteration. This cheap operation can be easily performed using a Newton step, for instance. Once the solution $\tilde{x}$ of the subproblem (5) is determined, the value of the objective function recomputed at the new point $\tilde{x}$ is then included in the set of sample points to replace x_{far}, the farthest point from $\tilde{x}$. This promotes inclusion of promising points in the set of sample points, thus improving the quality of the model. The radius of the trust region is then updated. The efficiency of the model is evaluated as follows:

$$e_k = \frac{f(\tilde{x}) - f(x_k)}{q_k(\tilde{x}) - q_k(x_k)} \tag{6}$$

If it is satisfactory, i.e., $e_k > \alpha$ (e.g., $\alpha = 0.8$), the trust region radius is increased because the model seems to be accurate and a larger step may be taken. If the efficiency is poor, i.e., $e_k < \beta$ (e.g., $\beta = 0.1$), the radius is reduced. Finally, the procedure goes on using the updated model and trust region. The algorithm is fully analyzed and validated for several problems in the paper by Marazzi and Nocedal [17].

5 Mesh Refinement Study

A grid refinement study is first performed on a typical configuration to determine how fine the mesh should be to obtain an accurate representation of the controlled flow. To this end, flows obtained on grids with different refinement levels are compared. A synthetic jet of width $h = 0.5\%\, l$ is arbitrarily located at 20% of the chord l of a NACA 0012 airfoil. The Reynolds number is $\text{Re} = 2 \times 10^6$, and the angle of attack is set to 18 deg. The nondimensional actuation frequency is $N_{\text{jet}} L / U_\infty = 1$, whereas the nondimensional amplitude of the jet is $U_{\text{jet}} / U_\infty = 1$. The angle of the jet direction with respect to the wall is $\alpha_{\text{jet}} = 30$ deg. The flow is initialized using the fields obtained from a previous simulation without actuation. The nondimensional time step is $\Delta t = 0.002$, which ensures an accurate description of each flow cycle. Turbulence is modeled with the $k-\omega$ SST model of Menter [10]. Flow computations are performed on four grids. The first grid is the baseline mesh $\mathcal{M}_0$. It is composed of 66,110 quadrangle cells in the vicinity of the airfoil and its wake, and triangles in the rest of the domain (see Fig. 4). The distance between the first point and the wall corresponds to $y^+ = 0.2$. The second grid $\mathcal{M}_1$ is the one-generation grid anisotropically refined in the tangential direction in a sphere of radius $5\%\, l$ centered at the jet center. The third grid $\mathcal{M}_2$ is the two-generation grid refined in two spheres of radius $5\%\, l$ and $4\%\, l$. The fourth grid $\mathcal{M}_3$ is the three-generation grid refined in three spheres of radius $5\%\, l$, $4\%\, l$, and $3\%\, l$ (see Fig. 5). Table 1 details the size of the grids and the number of faces on the jet boundary for each of them.

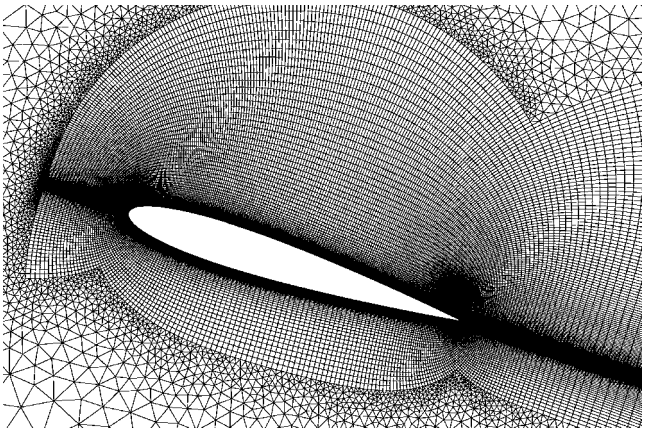

Fig. 4 Baseline grid

A comparison of the lift coefficient histories obtained with the different grids after all transient effects have vanished is shown in Fig. 6. As can be seen, results using grids $\mathcal{M}_2$ and $\mathcal{M}_3$ are very close to each other. This indicates that the two-generation grid $\mathcal{M}_2$ is fine enough to describe the actuated flow. Hence, we use this grid for the optimization problem detailed in Sec. 6.

6 Optimization of the Jet Location

6.1 Presentation of the Test Case. Now that computations with adaptive grids rely on a safe basis, we turn to optimization problems. The physical configuration of the problem as well as the numerical parameters are identical to those used for the grid refinement study. However, we consider two angles of attack, 18 deg and 20 deg, to quantify the influence of the angle of attack on the optimal actuator location.

The flow without actuation is characterized by a steady recirculation zone located at the trailing edge for the incidence 18 deg. Two steady vortices are present on most of the suction side of the airfoil for the incidence 20 deg (Fig. 7). Actually, these configurations correspond to flows at maximum lift and just after stall (Fig. 8).

The characteristics of the actuator are also the same as those used for the grid refinement study, except for the incidence of 20 deg for which the jet amplitude is increased to $U_{\text{jet}} / U_\infty = 1.5$. Lower values yield poor control at this incidence. The initial jet location is arbitrarily set to $s_0 = 20\%\, l$.

Finding an optimal jet location requires about 15 time-accurate flow simulations. For each one, time integration is carried out until a nondimensional time $t = 25$, to ensure that transcient effects have vanished. This requires roughly 500 CPU hours for each single optimization procedure.

6.2 Lift Enhancement. Lift enhancement obtained at both incidences is shown in Fig. 8 for a synthetic jet located at the initial and optimal positions. For an angle of attack of 18 deg, the lift increases only by $\sim 5\%$ with respect to the baseline airfoil. This is likely due to the fact that computations were performed in the vicinity of the maximum lift for the baseline airfoil. The actuation effects for the initial and optimized jet locations look similar. Actually, the initial point appears to be very close to the optimal one. However, for an angle of attack of 20 deg (post-stall regime), the results exhibit larger improvements. The lift increases due to the jet actuation by $\sim 43\%$ for the initial location and 57% for the optimized location. Thus, the benefit obtained by optimizing the jet location is clearly established for this case.

The time-averaged lift evolution with respect to the jet position

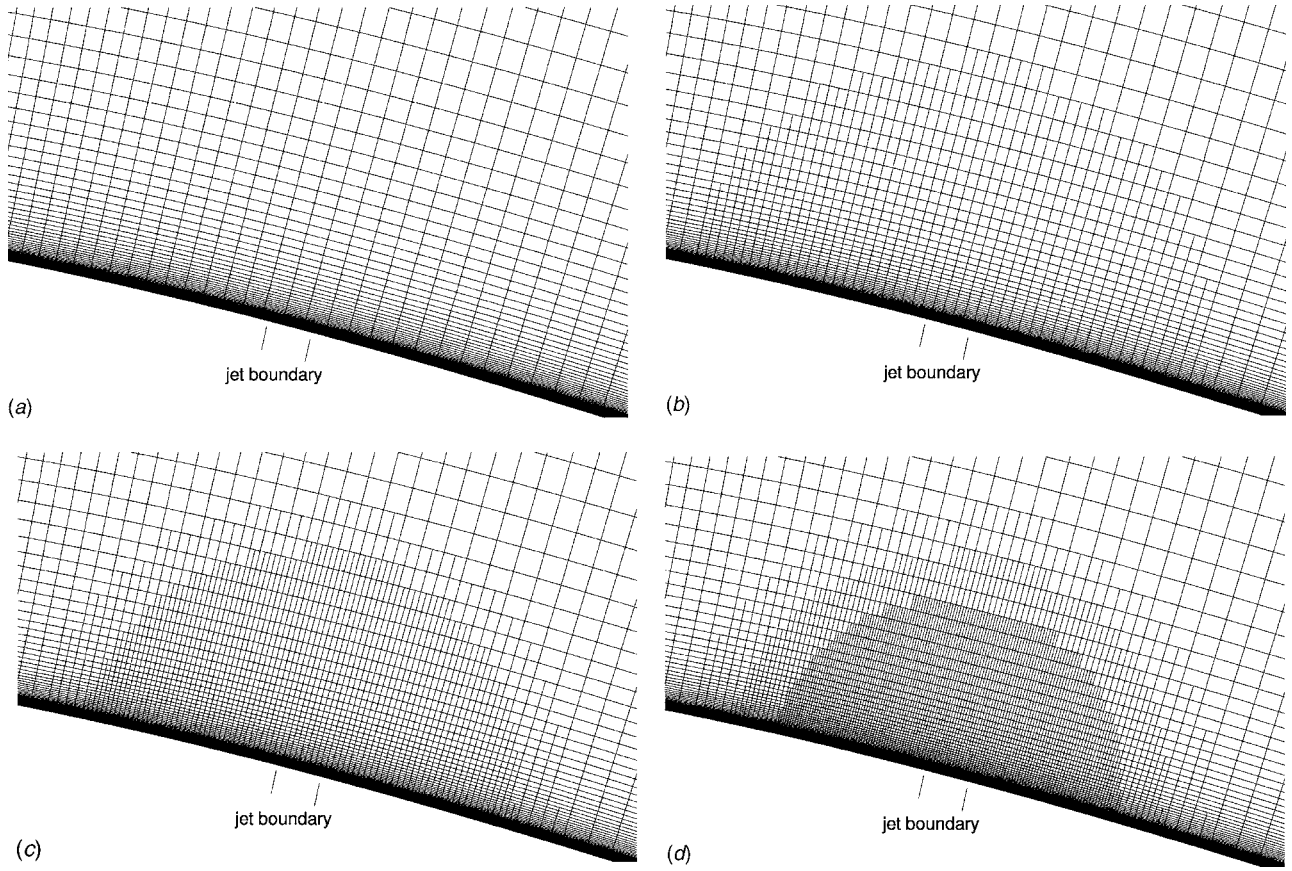

Fig. 5 Successive refined grid

is shown in Fig. 9. The evolution of the lift for an angle of attack of 18 deg is rather smooth, and the maximum is reached for $s_{\text{opt}}^{18}=0.23l$. The low variations of the lift can be explained in two ways: First, the incidence is close to the maximum lift incidence for the baseline airfoil. Thus, only moderate gains can be expected so that the amplitude of the synthetic jet is quite low. For an angle of attack of 20 deg, the influence of the actuator location on the lift is much larger. Thus, the optimization of the jet location yields significant improvements of the control efficiency. The maximum is reached for $s_{\text{opt}}^{20}=0.14l$, which is closer to the leading edge than in the previous case. However, the lift evolution exhibits some oscillations in the vicinity of the optimal location. The source of these oscillations is unclear. They may be due to a physical phenomenon yielding local optima caused by the strong nonlinearity of the flow in the vicinity of the synthetic jet. They may also be due to modeling uncertainties, since turbulence modeling using URANSE in the presence of a synthetic jet is still questionable. Additional flow analyses were performed a posteriori with actuator positions close to those for which oscillations were observed. They confirmed the occurrence of sudden lift variations as the jet is moved. Yet, no satisfactory explanation of their origin was found.

Table 1 Grids size

Mesh	Number of cells	Jet boundary faces
$\mathcal{M}_0$	66,110	2
$\mathcal{M}_1$	68,116	5
$\mathcal{M}_2$	71,401	8
$\mathcal{M}_3$	76,429	16

6.3 Flow Analysis. Flows are now analyzed to understand how the jet location influences the control efficiency. The temporal evolutions of the lift coefficient along one flow period are depicted in Figs. 10 and 11 for both incidences. Three jet locations are considered:

- upstream of the best location: $s=10\%l$ for both incidences
- at the best location: $s_{\text{opt}}^{18}=23\%l$ and $s_{\text{opt}}^{20}=14\%l$

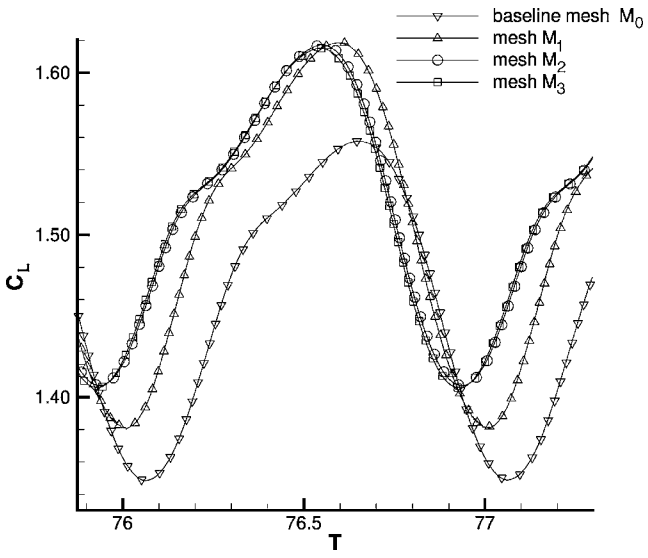

Fig. 6 Grid refinement study

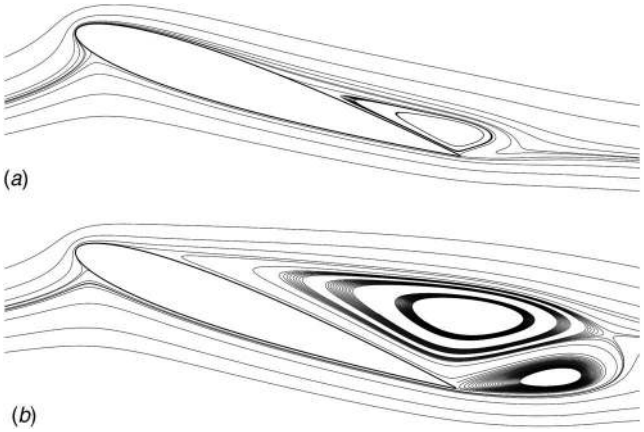

Fig. 7 Streamlines without actuation

- downstream the best location: $s=30\%l$ for an incidence of 18 deg and $s=20\%l$ for an incidence of 20 deg

Jet blowing is also presented in Figs. 10 and 11 to correlate it with lift evolution. Figures 12–15 show the pressure coefficient on the airfoil at maximum and minimum lift times for the three jet locations described above. Finally, Figs. 16–21 show streamlines at maximum and minimum lift times for the same jet locations. The arrow indicates the precise jet location on the airfoil.

6.3.1 Incidence 18 deg

From $s=10\%l$ *to* $s_{\text{opt}}^{18}=23\%l$. The lift histories (Fig. 10) show that the minimum lift value increases as the jet is moved downstream from $s=10\%l$ to $s_{\text{opt}}^{18}=23\%l$. This lift increase is caused by the suction peak enhancement (Fig. 13). This behavior can be explained by the fact that the minimum lift time, which corresponds to vortex shedding (Figs. 16(*b*) and 17(*b*)), is moved from blowing times to suction times (Fig. 10). Indeed, the suction peak is enhanced when the jet is in suction mode and reduced as it is blowing. Therefore, the increase of the minimum lift can be explained by a switch of the phase between the blowing/suction and the vortex shedding, due to the modification of the jet location.

The maximum lift is maintained (Fig. 10), as the jet is moved downstream. At the maximum lift time, a vortex is growing on the suction side of the airfoil for $s=10\%l$ (Figs. 16(*a*)), yielding an increase of the pressure level on the suction side (Fig. 12), whereas for $s_{\text{opt}}^{18}=23\%l$ the flow is still attached until the trailing

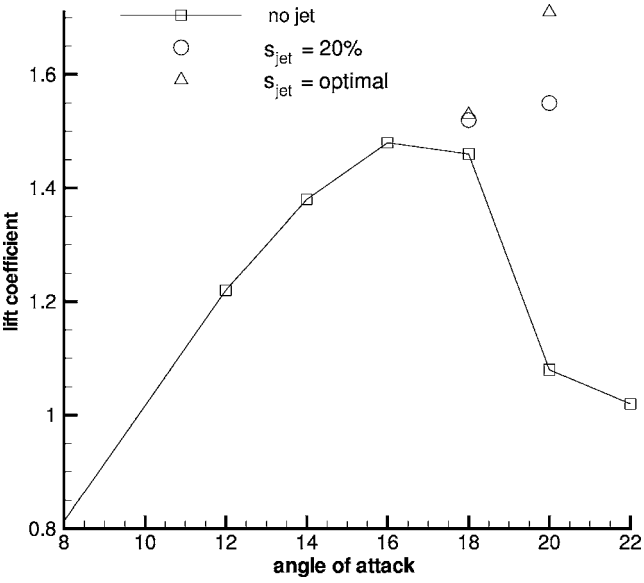

Fig. 8 Lift coefficient with respect to the angle of attack

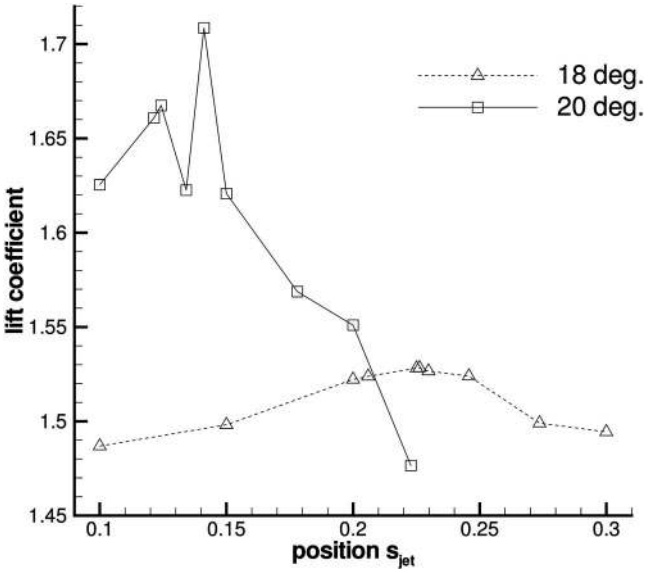

Fig. 9 Lift coefficient with respect to the jet position

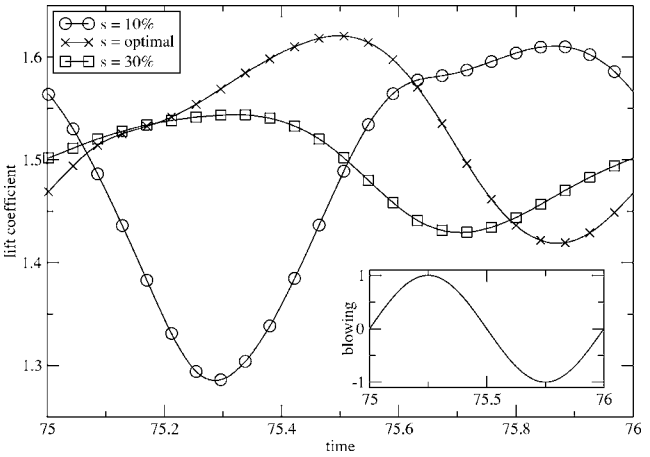

Fig. 10 Lift coefficient history for incidence 18 deg

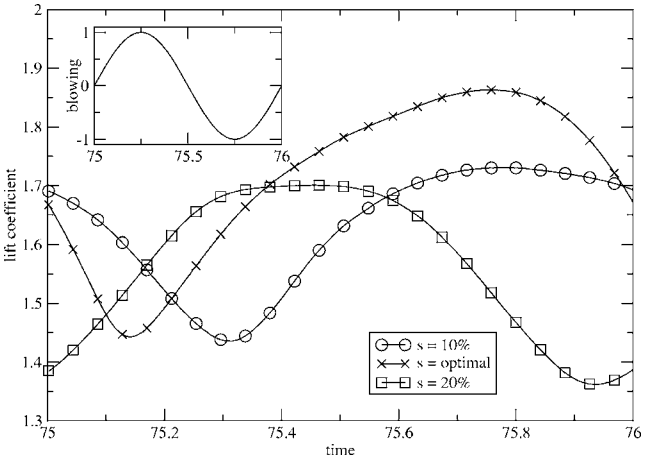

Fig. 11 Lift coefficient history for incidence 20 deg

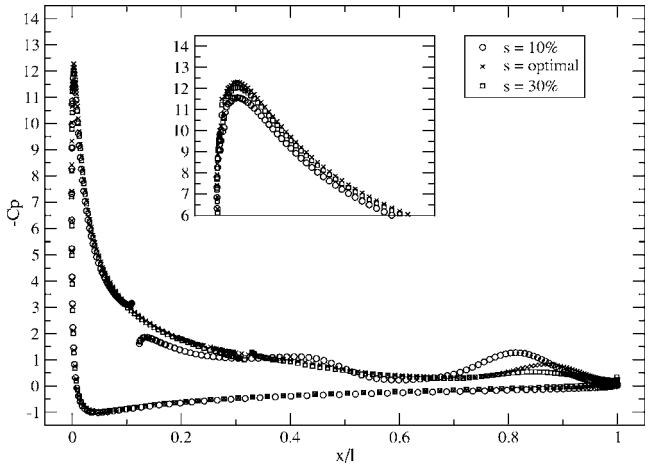

Fig. 12 Pressure coefficient at the maximum lift time for incidence 18 deg

edge (Fig. 17(*a*)), yielding a lower pressure level on the suction side, particularly at the suction peak. Nevertheless, this improvement is balanced by a slight suction effect in the vicinity of the vortices for $s=10\%l$ (Fig. 12), due to a more intense vorticity

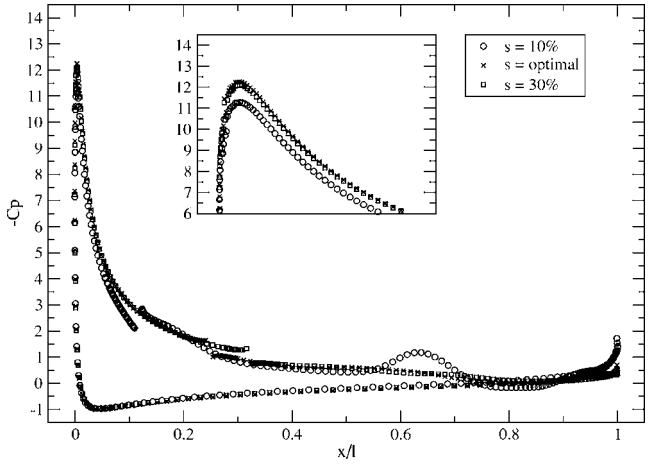

Fig. 13 Pressure coefficient at the minimum lift time for incidence 18 deg

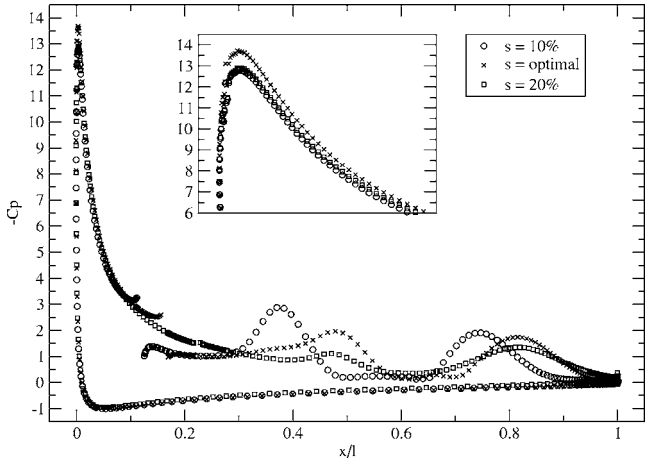

Fig. 14 Pressure coefficient at the maximum lift time for incidence 20 deg

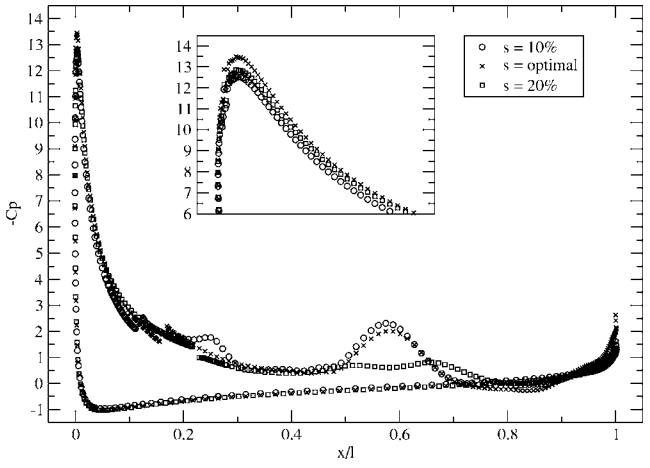

Fig. 15 Pressure coefficient at the minimum lift time for incidence 20 deg

(Figs. 16(*a*)). Moreover, the suction effect of the jet for $s=10\%l$ at this time compensates the high level pressure at the suction peak explained previously. Finally, the lifts for the two locations are quite similar.

From $s^{18}_{\text{opt}}=23\%l$ *to* $s=30\%l$. The lift histories (Fig. 10) show that the minimum lift value is globally maintained as the jet is

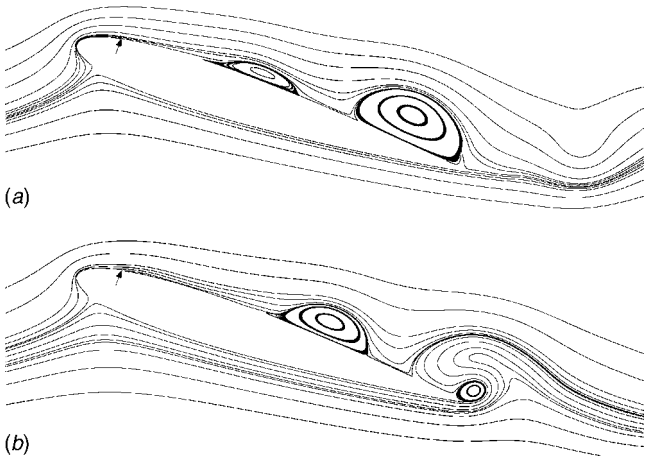

Fig. 16 Incidence 18 deg, $s=0.1l$

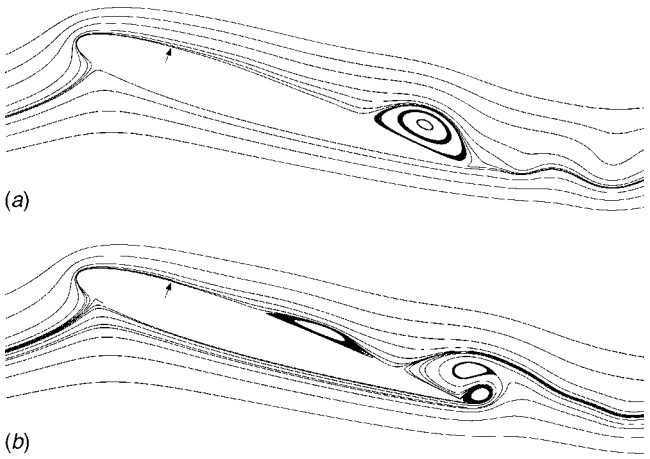

Fig. 17 Incidence 18 deg, $s=s^{18}_{\text{opt}}$

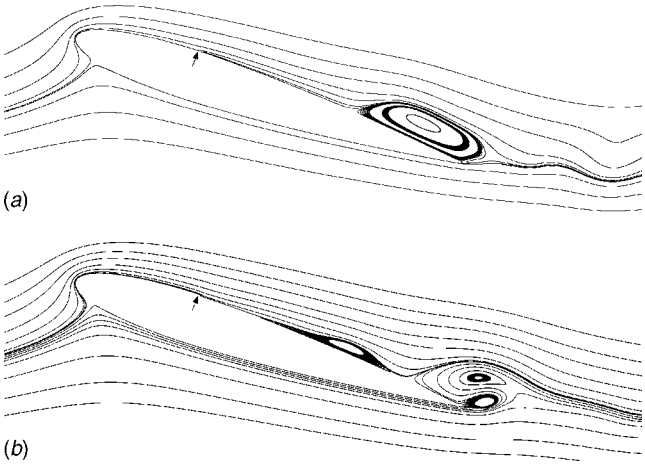

Fig. 18 Incidence 18 deg, $s=0.3l$

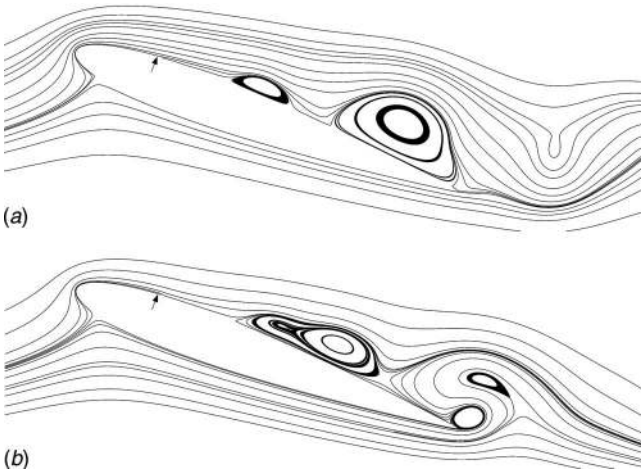

Fig. 21 Incidence 20 deg, $s=0.2l$

moved downstream from $s_{opt}^{18}=23\%l$ to $s=30\%l$, whereas the maximum lift decreases. At the minimum lift time, the suction peak enhancement due to the jet suction is slightly reduced because the jet location is moved downstream since the distance between the jet and the suction peak increases (Fig. 13). However, this effect is balanced by the fact that the growing vortex is delayed for $s=30\%l$ (Figs. 17(*b*) and 18(*b*)). At the maximum lift time, the lift decrease can be explained by a larger vortex located at the trailing edge for $s=30\%l$ (Figs. 17(*a*) and 18(*a*)).

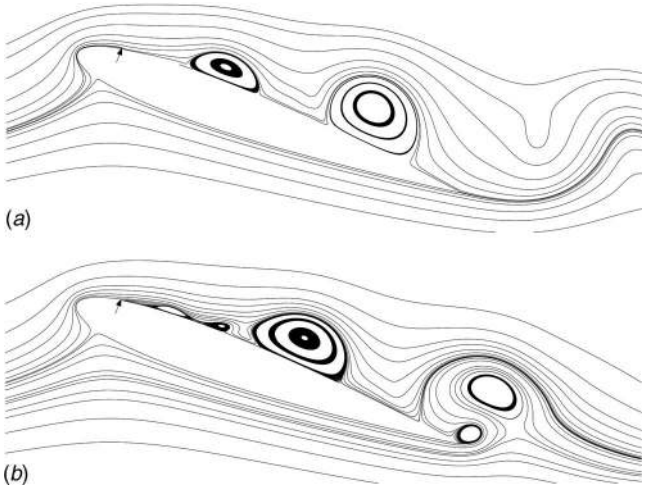

Fig. 19 Incidence 20 deg, $s=0.1l$

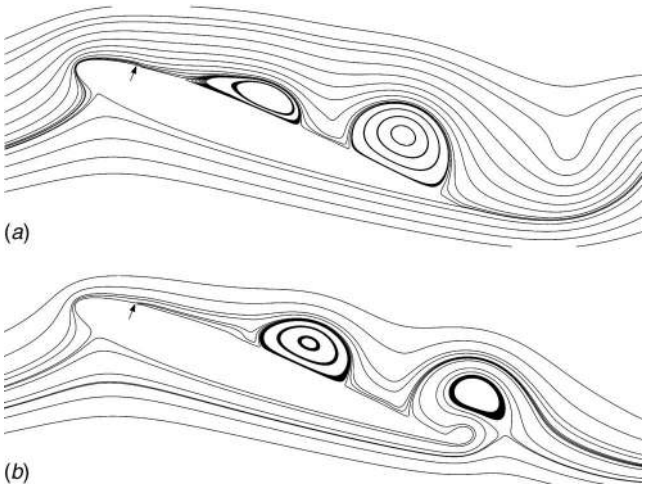

Fig. 20 Incidence 20 deg, $s=s_{opt}^{20}$

6.3.2 Incidence 20 deg

From $s=10\%l$ *to* $s_{opt}^{20}=14\%l$. As can be seen in Fig. 11, the minimum lift is maintained as the synthetic jet is moved from $s=10\%l$ to $s_{opt}^{20}=14\%l$. For $s=10\%l$, vortices are generated very close to the leading edge (Fig. 19(*b*)) yielding a decrease of the suction peak (Fig. 15). This is not the case for $s_{opt}^{20}=14\%l$ (Fig. 20(*b*)). However, this change is balanced by a slight pressure decrease at the vortices' locations for $s=10\%l$, due to a more intense vorticity field (Figs. 15 and 19(*b*)). Finally, the lift curves are similar for the two jet locations.

The maximum lift is far higher for the optimized jet location (Fig. 11). The pressure distribution along the airfoil clearly shows that this is due to the enhancement of the suction peak as the jet is moved downstream (Fig. 14). For $s=10\%l$, the vortex is located slightly closer to the leading edge (Fig. 14), yielding a decrease of the level of the suction peak.

From $s_{opt}^{20}=14\%l$ *to* $s=20\%l$. As the jet is moved downstream from $s_{opt}^{20}=14\%l$ to $s=20\%l$, both maximum and minimum lifts are decreased. Indeed, at the minimum lift time, the flow is detached over more than half of the suction side of the airfoil for $s=20\%l$, including low intensity vortices (Fig. 21(*b*)) and yielding a flat pressure distribution (Fig. 15). Hopefully, the effect is partially balanced by the enhancement of the suction peak due to the sucking jet. At the maximum lift time, the lift is lower for $s=20\%l$ than for $s_{opt}^{20}=14\%l$, since vortices have a lower intensity and the jet is blowing, which result in a lower suction effect at the vortices' locations as well as at the suction peak (Fig. 14).

6.4 Synthesis. These results lead us to propose some key ideas to explain the control efficiency changes as the synthetic jet is moved along the suction side of the airfoil:

- Enhancement of the suction peak by the jet—If the synthetic jet is located close to the leading edge, it excites the suction peak: during the jet-suction phase, the suction peak is enhanced, whereas during the jet-blowing phase, the suction peak is reduced. This mechanism weakens as the jet is moved downstream.
- Temporal phase between the vortex shedding and the suction/blowing effects—For some jet locations, vortex shedding occurs in phase with the suction peak enhancement by the sucking jet. Then, the lift decrease due to the

vortex shedding is compensated by a higher suction peak.
- Location of the vortices' birth—As the synthetic jet is moved upstream, the location where vortices are generated moves upstream as well. It results in a pressure increase at the suction peak and a decrease of the lift.
- The intensity of vortices.

If the synthetic jet is located close to the leading edge, the vortices generated are more intense, causing a stronger suction effect as they move along the airfoil.

Conclusion

A methodology for automatically finding the optimal location of a synthetic jet is proposed by coupling of a time-accurate flow solver, an adaptive mesh refinement/coarsening technique, and an optimization algorithm. Unsteady Reynolds-averaged Navier-Stokes equations (URANSE) are solved with a near-wall low-Reynolds number turbulence closure to obtain the controlled flow around the airfoil. An unstructured grid refinement/coarsening method is used to automatically generate meshes adapted to the presence of the synthetic jet. Finally, an optimization algorithm searches for the best location of a synthetic jet to maximize lift.

This methodology is demonstrated by optimizing the location of a synthetic jet on the suction side of the NACA 0012 airfoil for a Reynolds number $\mathrm{Re}=2\times10^6$ at incidences of 18 deg and 20 deg for stall control purposes. Results show that the influence of the jet location on the control efficiency is moderate at the incidence of 18 deg. However, the jet location has a stronger effect at an incidence of 20 deg. At this angle, lift increases by +43% for the initial jet location and by +57% for the optimal location. Then, the usefulness of the proposed approach is demonstrated. One can also note that the optimal locations found at the incidences 18 deg and 20 deg are different.

Analysis of the controlled flows yields guidelines for practical jet positioning: enhancement of the suction peak by the jet, the temporal phase between the vortex shedding and the suction/blowing effects, the location of the vortices' birth, and the intensity of the vortices seem to have a critical influence on the control efficiency.

References

[1] Seifert, A., Darabi, A., and Wygnanski, I., 1996, "Delay of Airfoil Stall by Periodic Excitation," AIAA J., **33**(4), pp. 691–707.

[2] Wu, J. M., Lu, X. Y., Denney, A. G., Fan, M., and Wu, J. Z., 1997, "Post-stall Lift Enhancement on an Airfoil by Local Unsteady Control. Part i. Lift, Drag and Pressure Characteristics," AIAA Paper No. 97–2063.

[3] Donovan, J. F., Kral, L. D., and Cary, A. W., 1998, "Active Flow Control Applied to an Airfoil," AIAA Paper No. 98–0210.

[4] Ekaterinaris, J. A., 2003, "Active Flow Control of Wing Separated Flow," ASME FEDSM'03 Joint Fluids Engineering Conference, Honolulu, HI, USA.

[5] Duvigneau, R., and Visonneau, M., 2004, "Simulation and Optimization of Aerodynamic Stall Control Using a Synthetic Jet," 2nd AIAA Flow Control Conference, Portland, AIAA Paper No. 2004-2315.

[6] Duvigneau, R., and Visonneau, M., 2006, "Optimization of a Synthetic Jet Actuator for Aerodynamic Stall Control," Comput. Fluids, **35**, pp. 624–638.

[7] Demirdžić, I., and Muzaferija, S., 1995, "Numerical Method for Coupled Fluid Flow, Heat Transfer and Stress Analysis Using Unstructured Moving Meshes With Cells of Arbitrary Topology," Comput. Methods Appl. Mech. Eng. **125**, pp. 235–255.

[8] Rhie, C. L., and Chow, W. L., 1982, "A Numerical Study of the Turbulent Flow on an Isolated Airfoil With Trailing Edge Separation," AIAA/ASME 3rd Joint Thermophysics Fluids, Plasma and Heat Transfer Conference, AIAA Paper No. 82-0998.

[9] Issa, R. I., 1985, "Solution of the Implicitly Discretized Fluid Flow Equations by Operator-Splitting," J. Low Temp. Phys., **62**, pp. 40–65.

[10] Menter, F. R., 1993, "Zonal Two-Equations $k-\omega$ Turbulence Models for Aerodynamic Flows," AIAA Paper No. 93-2906.

[11] Hay, A., and Visonneau, M., 2005, "Adaptive Mesh Strategy Applied to Turbulent Flows," C. R. Acad. Sci., Ser. Mecanique, **333**(1), pp. 103–110.

[12] Hay, A., Leroyer, A., and Visonneau, M., 2006, "H-Adaptive Navier-Stokes Simulations of Free-Surface Flows Around Moving Bodies," J. Mar. Sci. Technol., **11**(1), pp. 1–18.

[13] Duvigneau, R., and Visonneau, M., 2001, "Shape Optimization for Incompressible and Turbulent Flows Using the Simplex Method," AIAA Paper No. 2001-2533.

[14] Duvigneau, R., Visonneau, M., and Deng, G. B., 2003, "On the Role Played by Turbulence Closures for Hull Shape Optimization at Model and Full Scale," J. Mar. Sci. Technol., **8**(1), pp. 11–25.

[15] Hay, A., and Visonneau, M., 2005, "Local Mesh Adaptation and Remeshing Technique Applied to a Multiple Element Airfoil," 17th AIAA Computational Fluid Dynamics Conference, Toronto, Ontario, Canada, AIAA Paper No. 2005-5337.

[16] Nielsen, E. J., and Anderson, W. K., 1999, "Aerodynamic Design Optimization on Unstructured Meshes Using the Navier-Stokes Equations," AIAA J., **37**(11), pp. 1411–1419.

[17] Marazzi, M., and Nocedal, J., 2002, "Wedge Trust Region Methods for Derivative Free Optimization," Math. Program., **91**(2), pp. 289–305.